Sensors and Actuators B 254 (2018) 561–572

Contents lists available at ScienceDirect

Sensors and Actuators B: Chemical

journal homepage: www.elsevier.com/locate/snb

A zone-heated gas chromatographic microcolumn: Energy efficiency

Zhijin Lin[a,d,1], Nicolás Nuñovero[a,d,1], Junqi Wang[b,d], Robert Nidetz[c,d], Sanketh Buggaveeti[c,d], Katsuo Kurabayashi[c,d], Edward T. Zellers[a,b,d,*]

[a] Department of Environmental Health Sciences, University of Michigan, Ann Arbor, MI 48109-2029, USA
[b] Department of Chemistry, University of Michigan, Ann Arbor, MI 48109, USA
[c] Department of Mechanical Engineering, University of Michigan, Ann Arbor, MI 48109, USA
[d] Center for Wireless Integrated MicroSensing & Systems (WIMS2), University of Michigan, Ann Arbor, MI, USA

ARTICLE INFO

Article history:
Received 24 April 2017
Received in revised form 1 July 2017
Accepted 12 July 2017
Available online 18 July 2017

Keywords:
Microcolumn
MicroGC
Zone heating
Band trajectory modeling
Separation

ABSTRACT

A microfabricated separation column designed for ultimate use in a wearable gas chromatographic micro-analytical system (μGC) for analyzing mixtures of airborne volatile organic compounds (VOC) is described. The monolithic μcolumn chip measures 7.1 × 2.7 × 0.075 cm and contains a 6-m long, 250 × 140 μm deep-reactive-ion-etched Si channel with a Pyrex cap, wall-coated with a polydimethylsiloxane (PDMS) stationary phase. Along the channel are three serial 2-m long spiral segments, each with an independent integrated resistive heater and thermal isolation features etched in the substrate. By turning the segment heaters on and off at strategic points during a separation, significant energy savings could be realized relative to heating the entire chip simultaneously (i.e., globally), with no loss in chromatographic resolution. A classical lumped element model was used as the basis for simulations of energy consumption, and a published band trajectory model was used to estimate analyte residence times in each segment. Four simple mixtures of volatile organic chemicals were used to evaluate the models and assess the energy consumed for zone heating and global heating under isothermal and temperature-ramped conditions. Modeled reductions in the required energy per analysis using zone (vs. global) heating ranged from 14 to 31% among the cases considered, depending on the heating profile (i.e., isothermal or ramped), heating schedule, and the retention times of the analytes in the mixture. Modeled energy reductions tended to underestimate experimental reductions, but differed by <2% in all cases considered. This approach to μcolumn design and operation shows promise for extending battery life in wearable μGC instrumentation.

1. Introduction

Gas chromatography (GC) is the method of choice for analyzing mixtures of airborne volatile organic compounds (VOC) [1]. In bench scale GC, a solution of the VOC mixture in a volatile solvent is injected into a heated separation column, typically between 100 and 530 μm in diameter, from 15 to 60 m in length, and wall-coated with a polymeric stationary phase (e.g. polydimethylsiloxane, PDMS). The mixture components are then separated by virtue of differential partitioning as they are transported down the length of the column under pressure driven flow of an inert carrier gas. One of several types of detectors is used to quantify the compounds eluting from the end of the column by measuring the integrated peak area or peak height. Where a single-channel detector is used, retention time (t_R) is used to identify the compound (via prior calibration with known standards). Where a mass spectrometer (MS) is used as the detector, the identification is enhanced by use of the fragmentation spectrum [1].

Field portable GC instrumentation is available for applications where direct, on-site analysis is needed [2–8]. For field deployment, numerous instrument modifications are necessary; for example, some inlets are adapted for automatic sample collection and injection, shorter columns are typically used, and various approaches are employed to reduce size, weight, and power for heating components and fluidic interconnects. Reliable analyses of VOC mixtures are achievable, yet the relatively large size, high cost, and high power requirements preclude routine or long-term deployment, particularly where battery power is required.

In response, numerous efforts have been mounted over the past four decades to create portable GC instruments that use microfab-

* Corresponding author at: Department of Environmental Health Sciences, University of Michigan, Ann Arbor, MI 48109-2029, USA.
E-mail address: ezellers@umich.edu (E.T. Zellers).
[1] These co-authors contributed equally.

http://dx.doi.org/10.1016/j.snb.2017.07.065
0925-4005/

ricated components (μGC) [3,6,9–19], some of which have been commercialized [3,6]. Typical microfabricated components include an adsorbent-packed preconcentrator or loop sampler that also serves as an injector, one or more etched channels with wall-coated stationary phases that serve as separation columns, and a detector consisting of either an individual sensor or an array of sensors the collective output of which may provide a response pattern that can enhance analyte recognition. Although the reductions in size (mass) associated with microfabrication lead to commensurate reductions in heating power requirements, overall power demands in reported μGC systems remain high and represent a limiting factor in simultaneously meeting goals of high performance, miniaturization, and long-term battery operation.

The μcolumn is a critical component of any μGC, and numerous approaches to μcolumn chip design and operation have been reported to address the challenges of maintaining high resolution, sample capacity, and peak capacity over the inherently short separation distances available [20–30]. Although the power required for heating chip-based μcolumns is generally lower than that of conventional capillary columns due to their compact size and use of thin, integrated resistive heating elements, only a few μcolumn development efforts have focused on designs where power efficiency was an overriding priority [23,25].

We are currently developing a μGC prototype, referred to as a personal exposure monitoring microsystem (PEMM), small enough to be worn by workers in industrial settings to measure their exposures to VOC mixtures [31]. The PEMM is battery powered and expected to perform several analyses per hour for at least 8 h/day. Therefore, the power requirements of the system are critically important. Since the separations require heating the μcolumn for a significant fraction of a typical sampling and analytical duty cycle, reducing the power required to heat the μcolumn can lead to significant reductions in the energy per analysis.

Toward that end, we conceived of a μcolumn in which sequential heating of each of three segments (or zones) is used. We hypothesized that with proper design and operation such a μcolumn could offer the same, or better, chromatographic resolution as that obtained with simultaneous (i.e., "global") heating of the entire μcolumn at once, but with less power. The concept is straightforward: whether operating isothermally or with temperature programming, by turning on and off the heaters serving each segment (or zone) according to the needs of the separation, less power would be needed, provided that sufficient thermal isolation could be achieved between segments.

In contrast to multiple μcolumn systems [15,16,32–36], which require heated interconnections and fluidic transitions that increase complexity and invariably incur losses in performance or power efficiency (in exchange for modularity), the segmented μcolumn considered here is monolithic. In contrast to the parallel (i.e., concentric) 3-channel μcolumn reported by Lu and coworkers for use in their multidimensional separation subsystem, which was also monolithic [36], our μcolumn is a single channel with each segment adjacent to, and partially isolated thermally from, the next to permit nearly independent heating. Although thermal gradient μGC (μTGGC), such as reported by Wang et al. [37] and Navaei, et al. [38], could ostensibly be implemented with a segmentally heated μcolumn, the design pursued here was not intended for μTGGC and would not be amenable to it due to the use of a convolved spiral microchannel layout within each segment wherein the flow direction changes in each adjacent microchannel within the spiral. We are unaware of prior work on a μcolumn of this design or of attempts to use zone heating to take advantage of the microchannel density and low mass inherent in etched-channel μGC columns.

In this article, we describe the design, fabrication, modeling, and initial characterization of a monolithic μcolumn having three partially isolated segments, each with an independent heater, capable of segment/zone heating. Focus is placed on energy efficiency, rather than chromatographic efficiency, per se. The latter will be dealt with in a subsequent publication. Finite element thermal modeling was performed to optimize the design of the heaters and a classical lumped-element model that accounts for inter-segment heat transfer was used to estimate power and energy dissipation. The migration times of compounds in the μcolumn were estimated by adaptation of a published band trajectory model (BTM) [39]. The accuracies of the latter models were evaluated and both the chromatographic resolution and energy requirements of zone heating vs. global heating were assessed for isothermal and temperature programmed separation conditions.

1.1. Band trajectory model (BTM)

Implementation of such an approach to μcolumn design and operation requires knowledge of the locations of eluting compounds along the channel, and thus in each segment, over the course of a separation. Toward this end, we adapted the BTM reported by McGuigan and Sacks originally developed for use in dual-column, pressure-tuned ensembles [39]. The key expression from the model is given in Eq. (1):

$$t_{x'} = \sum_{0}^{x'} \frac{64\eta \cdot \Delta x \cdot (k-1)\sqrt{P_{i/o}^2 - (x/L)\left(P_{i/o}^2 - 1\right)}}{d^2 p_0 \left(P_{i/o}^2 - 1\right)} \quad (1)$$

where $t_{x'}$ is the total time required for an analyte band to migrate a distance, x' ($=x+\Delta x$), along the length, L, of the μcolumn, d is the effective inner diameter of the μcolumn, p_0 is the outlet pressure, $P_{i/o}$ is the inlet:outlet pressure ratio, η is the temperature-dependent viscosity of the carrier gas, and k is the temperature-dependent retention factor of the analyte. By dividing L into a series of incremental length intervals, Δx, Eq. (1) allows the trajectory of each analyte to be mapped over time. Values of η are available in the literature [40], and k can be determined empirically. A plot of time vs. distance gives the segment-specific retention times, t_R, needed to effectively implement the zone heating technique.

1.2. Thermal modeling

Assuming uniform temperature within each segment, i, the heating of the segments of the μcolumn can be represented by a classical lumped capacitance model [41,42], the equivalent circuit of which is given in Fig. 1, which considers three adjacent μcolumn segments, each with a heat capacity, C_i, thermal resistance, R_i, and source of power, P_i, that is capable of generating a certain rate of heat flow, dQ/dt, to the segment. The resistance to heat transfer between segments is R_c and the additional power required to compensate for such inter-segment heat transfer (i.e., thermal cross-talk) can be expressed simply as P_{ci}. According to this model, the power required to create a temperature difference above ambient, θ_i, is given by:

$$P_i = \frac{dQ}{dt} = C_i \frac{d\theta_i}{dt} + \frac{\theta_i}{R_i} + P_{ci} \quad (2)$$

where each R_i would be measured experimentally and therefore would implicitly account for convective heat transfer to the surroundings.

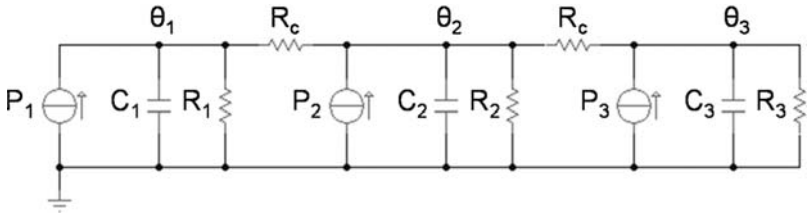

Fig. 1. Thermal model of the segmented column for zone heating energy analysis.

The energy, E_{ij}, consumed to raise the segment to a specified set-point temperature, θ_s, and maintain it there for some time period, t_j, as in an isothermal separation, can be expressed as

$$E_{ij} = \int_0^{t_j} P_i dt = C_i \theta_s + \frac{\theta_s}{R_i} t_j + E_{cij} \tag{3}$$

where E_{cij} accounts for the energy lost to the adjacent segments. If enough time elapses for steady-state conditions to be reached and maintained, then we can approximate E_{ij} as follows:

$$E_{ij} = P_i t_j = \left(\frac{\theta_s}{R_i} + \frac{\theta_c}{R_c} \right) t_j \tag{4}$$

where θ_c is the inter-segment temperature difference at steady state.

For the case of a linear temperature ramp, as is often employed in a temperature-programmed separation, θ_i, and therefore P_i, increase with time and the energy consumed can be expressed as

$$E_{ij} = C_i M t_j + \frac{M}{2R_i} t_j^2 + E_{cij} \tag{5}$$

where M is the temperature ramp rate. Since E_{ij} is a quadratic function of time and it also depends on C_i, a linear approximation like Eq. (4) no longer applies.

For the purpose of this analysis we next consider an isothermal separation and compare the total energy required to perform such a separation via zone heating of the individual segments, E_Z, to that required via "global" heating, E_G, where the three segments are heated simultaneously to achieve θ_s for the entire analysis time period, t_a. For the latter scenario, $\theta_c \approx 0$ (Eq. (4)), and assuming, for simplicity, that $R_1 = R_2 = R_3$, then we can express the total energy as

$$E_G = 3 \frac{\theta_s}{R} t_a \tag{6}$$

In the simplest zone heating scenario, there would be a sequence of three discrete time windows: t_1, when only segment 1 is heated; t_2 when only segment 2 is heated (segment 1 is turned off); and t_3 when only segment 3 is heated (segment 2 is turned off). The sum of these t_i values is t_a, and for the special case where $t_1 = t_2 = t_3$, the segment heating time is t_s. Regardless of the duration of each time window, if we consider the ideal situation where R_c is infinitely large, then the E_Z/E_G is 0.33 and the energy reduction from zone heating is 0.67 (i.e., 67%). This represents the maximum possible energy savings.

In fact, this simple case would rarely occur in practice because it requires that the analytes migrate in close proximity throughout the separation. Normally, there would be a larger range of migration rates and associated retention times (and residence times) such that some analytes would be present within all three segments for a significant portion of time. Acknowledging this, another isothermal scenario can be considered for which we designate five discrete time windows ($t_1 - t_5$), wherein heating of the first segment for t_1 would be followed sequentially by heating of the second and third segments for t_2 and t_3, respectively, all to the same θ_s. At the end of t_3, the first segment heating would be discontinued, and then at the end of t_4, the second segment heating would be discontinued. The last period (i.e., t_5) would extend to the point where the last compound elutes from the μcolumn, marking the end of the run, at $t = t_a$.

From Eq. (4) we can express E_Z as the sum of the energies consumed during each t_i, i.e.

$$E_Z = \sum_{i=1}^{3} \sum_{j=1}^{5} E_{ij} \tag{7}$$

and for any isothermal scenario we expect the migration rates of the analytes to be nearly constant throughout the separation (*vida infra*), so that each analyte spends an equal amount of time in each 2-m segment. Since the schedule of segment heater turn-on and turn-off times is specified by the retention time of the analyte of highest volatility (t_h) and the retention time of the analyte of lowest volatility (t_a), respectively, we can express the time windows t_j in terms of those limiting values (i.e. $t_1 = t_2 = t_h/3$, $t_3 = t_a/3 - 2t_h/3$, *and* $t_4 = t_5 = t_a/3$). If we designate the range of analyte retention times spanned in a given analysis as $\Delta t_R = t_a - t_h$, then we can express the fractional reduction in energy attributable to zone (vs. global) heating, E_R ($= 1 - E_Z/E_G$) as follows:

$$E_R = \left(1 - \frac{1}{3} \left(\frac{1}{1 + R_c/R} + \frac{1}{\left(1 + \left(1 + R_c/R \right)^{-1} \right)^{-1} + R_c/R} \right) \right) \left(\frac{2}{3} - \frac{\Delta t_R}{3 t_a} \right) \tag{8}$$

Eq. (8) shows the two main factors that influence the attainable energy savings due to zone heating. The first term on the right-hand side (within large parentheses) accounts for inter-segment thermal isolation, expressed as the ratio R_c/R. When R_c/R is «1 (i.e. poor isolation), this first term approaches zero and there would be little or no reduction in energy with zone heating. As R_c/R becomes larger, the term gradually approaches unity, following the trend shown in Fig. S1 of the online Supplementary Material (SM), and the energy reduction would be maximized with respect to this factor. Thus, the μcolumn should incorporate design features that increase R_c to the extent permitted by the physical constraints of the device structure and material properties.

The second term on the right-hand-side of Eq. (8) accounts for the fraction of the total separation time the segment heaters are off. As in the ideal scenario presented above, this term approaches its highest value of 2/3 when Δt_R ($= t_a - t_h$) is small, which would occur for a set of compounds with very similar retention times for which the three segment heaters could be switched on and off in succession (i.e. $t_s \approx t_a/3$). For a broader spectrum of compound retention times, Δt_R would be a larger fraction of t_a, the heating times of the segments would overlap, and E_R would decrease. This second term would approach its minimum value of 1/3 as Δt_R approaches t_a. However, even for modest values of t_h there would be delays in the turn-on of segment 2 and 3 heaters and commensu-

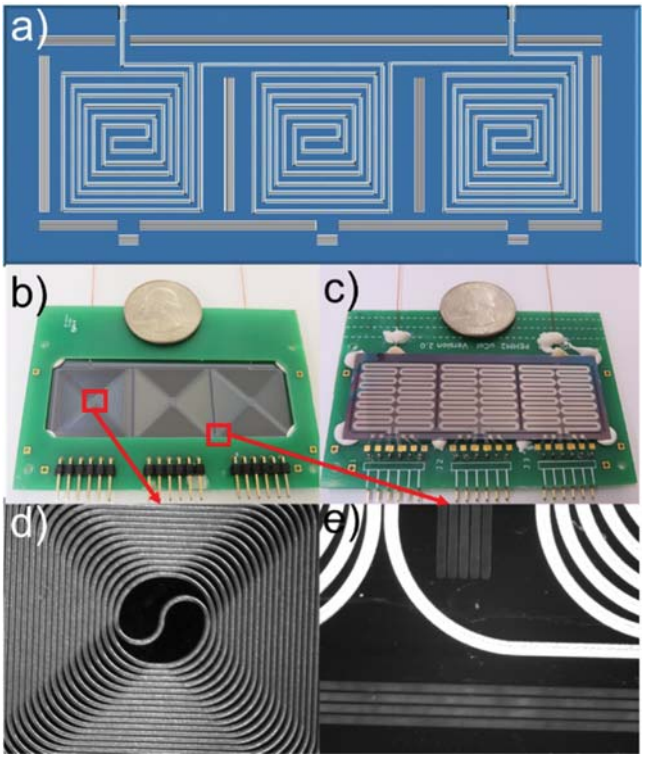

Fig. 2. (a) Concept diagram of the segmented μcolumn; (b) top-side view and (c) bottom-side view of the μcolumn mounted on its printed circuit (carrier) board, with the channel visible from the top side and heater patterns visible from the bottom; (d) enlargement of the center of the spiral of one μcolumn segment; (e) enlargement of the slot/fin thermal isolation structures.

rate savings of energy. In practice, the schedule of segment heating would be determined by the residence times of the mixture components in each segment, which could be accurately predicted by BTM (*vida supra*).

For the more complicated cases involving temperature programmed separations, account must be taken of the scheduling and durations of the different time windows, segment heating rates, minimum and maximum temperatures, and thermal capacitances, as well as the temperature dependence of thermal resistances, the use of PWM with feedback control, and the limited power available to actuate the heaters. Computer simulation was used to account for these factors using algorithms that allowed E_Z and E_G to be evaluated for any conceived heating scenario, as discussed below.

2. Materials and methods

2.1. Materials

All solvents, test compounds, and reagents were obtained from Sigma-Aldrich (Milwaulkee, WI) or Fisher Scientific (Fair Lawn NJ) in >98% purity and used as received. PDMS was purchased from Ohio Valley Specialty Company (OV-1, Marietta, OH). Deactivated fused-silica capillaries (intermediate polarity, 0.25 mm i.d.) and press-fit connectors were obtained from Supelco (Bellefonte, PA).

2.2. μColumn design, fabrication, and preparation

Fig. 2a shows the conceptual layout of the segmented Si μcolumn channel and thermal isolation structures. The pitch, cross section, length, and spiral patterns of the channel mimic those of the early μcolumns reported by Lambertus, et al. [20], and later versions on which we reported [9,14–16,28]. The chamfered-square spiral pattern (apparent in the micrograph in Fig. 2d, but not in Fig. 2b) offers a tighter packing than a circular-spiral or serpentine channel layout, and thus a smaller thermal mass. Chamfering the corners reduces turbulence and, thus, band dispersion.

The thermal isolation structures (Fig. 2e) consist of slots etched through the substrate with fins extending lengthwise within each slot to increase surface area for dissipating heat convectively to the ambient while reducing in-plane heat conduction. These are similar to those reported by Manginell, et al. for thermally isolating their μcolumn from a μsensor integrated on the same Si substrate [19]. The meander-line heater dimensions were designed to minimize temperature gradients across a segment while also minimizing power dissipation. Fluidic inlet and outlet ports are located on one edge of the chip, opposite that where the heater bonding pads are located, to facilitate integration into the PEMM prototype.

SolidWorks (Release 2014, Dassault Systems, Waltham, MA) and COMSOL Multiphysics (R4.2, Burlington, MA) were used for design and simulation purposes, respectively. Simulations accounted for Joule heating of the μcolumn segments and convective, radiative, and conductive heat losses. Several different slot and fin configurations were assessed, and the final configurations included tradeoffs related to fabrication, such as pattern fidelity and mechanical strength. Details have been omitted for brevity. For the final heater design, simulations indicated that the μcolumn would have thermal gradients of only ~1 °C across all segments when all three segments were heated to as high as 180 °C and only ~6 °C when heated individually.

The μcolumns were fabricated from 0.5-mm thick, 100-mm diameter, ⟨100⟩ double-side polished Si wafers (University Wafer, Boston, MA). First, a 1.5-μm thick layer of thermal SiO_2 was grown on both sides of the wafer. Then, the μcolumn channel (150 μm wide, 50 μm wall within spiral area), thermal isolation slots (600 μm wide) and fins (50 or 80 μm wide, spaced by 80 μm gaps) and expansion sections at the inlet and outlet of the channel (430 μm wide, 1950 μm deep) were defined photolithographically and the SiO_2 layer was reactive-ion-etched (RIE) to form a hard mask on the substrate (note: horizontal thermal-isolation slots have 3 fins, vertical slots have 4 fins, and the vertical fins at the outer edges of the chip are 80 μm wide while those between segments are 50 μm wide). A new layer of photoresist was then used to selectively pattern the fluidic expansion ports and slot struts on the front side, and deep reactive ion etching (DRIE) was used to etch these regions of the Si substrate to depth of 140 μm. The photoresist was then stripped and, using the initial SiO_2 hard mask, DRIE was used to create the μcolumn channel and to continue to etch the fins and inlets. DRIE was concluded once the μcolumns and inlets reached depths of 250 and 400 μm, respectively.

Next, the front-side oxide mask was selectively stripped with buffered HF, and then a 0.2-mm thick, 100-mm diameter Pyrex wafer was anodically bonded to the front side of the wafer, sealing the μchannel. Ti/Pt (30/360 nm) was then patterned on the backside using e-beam evaporation and liftoff to generate the heaters, resistive temperature devices (RTD), and dice lines. The fin structures were then patterned on the backside of the Si wafer and, after removing the oxide by RIE, DRIE was used to complete the thermal isolation slots and fins. Etched feature dimensions were confirmed throughout the fabrication process using a 3-D optical profiler (NewView 5000, Zygo, Middlefield, CT). Finally, the wafer was diced into μcolumns, and water and air were used to clean out dicing debris. Sections of deactivated fused-silica capillary (250 μm i.d.,) were inserted into the inlet and outlet ports and sealed with epoxy (Hysol 1C, Rocky Hill, CT).

The μcolumn was then statically coated with PDMS from a solution (4.38 mg/mL, methylene chloride/n-pentane, v/v = 1) that contained dicumyl peroxide (1% w/w of PDMS) as curing agent according to reported methods [19]. Briefly, the solution was drawn

through the μcolumn until the entire volume was filled. Then, one end was sealed with a septum, the μcolumn chip was placed in a water bath (30 °C) and gentle suction was applied to the other end to evaporate the solvent. The μcolumn was heated to 180 °C under N_2 atmosphere in a GC oven to cross link PDMS. On the basis of the internal surface area of the channel and the concentration of PDMS used, the average thickness of PDMS coated on the channel wall was 0.20 μm. The sections of interconnecting capillary, which were also coated and crosslinked, were cut to 4 cm.

The μcolumn was then affixed with a minimum of epoxy at each corner onto a printed circuit board (PCB) that had a slightly smaller rectangular hole cut out beneath the μcolumn chip, and the bonding pads for the heaters and RTDs were wire-bonded to the corresponding pads on the PCB. Additional epoxy was used to mechanically anchor the capillaries to the PCB. During testing the PCB was suspended by clips on a clamp-stand fixture.

2.3. μColumn characterization

All GC measurements were collected with a bench scale GC equipped with a flame ionization detector (FID) (Model 7890B, Agilent Technologies, Palo Alto, CA). The μcolumn was connected between the GC inlet and FID with sections of deactivated fused silica capillaries using press-fit connectors. GC injection port and detector temperatures were both 250 °C. For determinations of μcolumn efficiency the μcolumn temperature was controlled by the GC oven. For collecting k values used for BTM and for subsequent testing, the μcolumn temperature was controlled by the on-chip heaters.

For isothermal separations with global heating, all three heaters were turned on 35 s prior to the injection to allow all segments to come to the set-point temperature (note: this could have been done faster but there was need to do so for this set of tests). For temperature ramped separations with global heating all segments were ramped at the same rate to the same temperature. For isothermal separations with zone heating, segment heaters were turned on and off in sequence as dictated by BTM for the subset under test. For comparisons of global and zone heating retention times, the rate of heating was between 41 and 55 °C/min and segments were heated sufficiently early to achieve the set-point temperature at the required time. For comparisons of power dissipation between global and zone heating, segments were heated at 200 °C/min. For temperature ramped separations with zone heating, segments 2 and 3 were rapidly preheated in sequence to bring the segments to the temperatures needed to maintain the temperature ramp rate for the experiment.

The separation efficiency of the μcolumn was determined at 30 °C (GC oven) using n-octane as the probe by serial injections (splitless) with an autosampler and gas-tight syringe of headspace vapor from a septum-sealed vial containing liquid n-octane to which methane was added from the house supply. The adjusted retention times ($t_R' = t_R - t_M$) and full width at half-maxima ($fwhm$) of eluting peaks were measured as a function of average N_2 carrier gas velocity, where the hold-up time, t_M, was taken as the methane retention time. The average velocity was calculated as L/t_M. The plate number, $N = 5.545(t_R'/fwhm)^2$ and plate height, $H = L/N$, were calculated and the latter used to generate a Golay plot to determine the minimum plate height, H_{min}, and maximum plate count, N_{max}, at the optimal velocity (see Fig. S2, SM) [1].

Table 1 lists the test compounds along with their corresponding vapor pressures, p_v. They have been grouped into four subsets based roughly on p_v ranges for the purposes of testing (described further below). The fourth subset in Table 1 consists of one member from each of the first three other categories, so as to span the range of p_v values of the entire set of compounds – this is referred to as the "general" subset. Values of k ($= t_R'/t_M$) for each compound were determined individually at each of five temperatures between 30 and 100 °C. Autosampler syringe injections of 0.1 μL liquid samples (~10 mg/mL in CS_2) were performed with a 20:1 split at an inlet pressure of 13.5 PSI using He as carrier gas. The same conditions were used for subsequent experiments.

Table 1
List of test compounds, subset assignments, and vapor pressures, p_v.

Subset	#[a]	Compound	p_v (kPa)[b]
High	1	Trichloroethylene	6.25
	2	Toluene	3.78
	3	2-Hexanone	1.46
Medium	4	n-Octane	1.88
	5	Ethylbenzene	1.27
	6	3-Heptanone	0.187
Low	7	n-Nonane	0.59
	8	1,2,4-TMB	0.27
	9	n-Decane	0.191
General	1	Trichloroethylene	6.25
	4	n-Octane	1.88
	9	n-Decane	0.191

[a] Refers to peak assignment in Fig. 3.
[b] At 25 °C; Ref. [43].

For subsequent comparisons of zone vs. global heating, compounds were tested in the subsets shown in Table 1 under both isothermal and temperature-ramped conditions. The three segment RTDs were calibrated in the GC oven. A custom LabVIEW program run from a desktop computer was used to heat each segment independently by use of a proportional-integral-derivative (PID) feedback loop between the voltage applied to each heater and the set-point temperature or temperature ramp. Pulse-width-modulated (PWM) voltages were applied to the heaters through solid-state relays at 4 Hz. Isothermal separations were performed in 10 °C increments from 50 to 100 °C. Temperature programmed separations were performed from a baseline temperature of 30 °C in 10 °C/min increments from 10 to 60 °C/min to a final temperature of 100 °C.

2.4. Band trajectory modeling

For BTM (via Eq. (1)), values of log k were plotted against $1/T$ and linear regression models fitted to the data were used to obtain k values at intermediate temperatures. (see Fig. S3, SM; $r^2 > 0.998$ in all cases). Values of $P_{i/o}$ were calculated as the ratio of p_i/p_o where p_o was atmospheric pressure and p_i was the sum of p_o and the applied pressure at the GC injection port (13.5 PSI, displayed on workstation readout). Values of η for the He carrier gas were obtained from ref. 40.

The μcolumn was divided into 2.5-mm intervals (Δx in Eq. (1)). For accurate results it was necessary to account for the 4-cm long PDMS-coated capillary sections epoxied into the inlet and outlet of the chip, and the 23- and 33.5-cm long sections of deactivated interconnecting capillary extensions used, all of which were 250 μm i.d. Note that the PDMS-coated-Si μcolumn was assumed to have an i.d., equivalent to a circular channel with an i.d. of 206 μm.

2.5. Energy consumption simulations

In order to estimate the energy savings for all the different heating scenarios, the model represented by Fig. 1 was translated to a multiple-input/multiple-output (MIMO) dynamic system, with heating power values as inputs and segment temperatures as outputs, and simulated in a PID feedback loop using Matlab (version 8.5, MathWorks, Inc., Natick, MA). The scheme of the MIMO model used is given in Fig. S4 of the SM. The temperature set-point profile

directing each feedback loop was constructed on the basis of the time windows obtained for each case from the BTM analysis. The transfer function matrix of the system, containing the ratios of all the combinations of θ_i and P_i, was obtained in Matlab by applying frequency-domain analysis to the μcolumn thermal model via a Laplace transform.

The transfer functions were evaluated using the thermal parameters C_i, R_i, and R_c, which were estimated experimentally. Each feedback loop was also provided with a saturation block to properly account for the limit of the power imposed by the supporting system; the PEMM system uses a 24-V power supply, which gives a maximum of 5 W for μcolumn heating and limits the ramp rate to ~200 °C/min. For switching the segment heaters from the off state to the desired temperature, faster heating rates for shorter time periods were found to consume less energy than slower rates for longer periods. This heating rate was standardized to 200 °C/min for all simulations and experiments related to energy consumption estimation. Furthermore, for this study, we placed a conservative limit of 100 °C on the maximum μcolumn temperature, such that the maximum θ_i would be 70 °C, since 30 °C is the assumed baseline temperature inside the PEMM prototype. Under this constraint, separations were complete in <161 s in all cases.

2.6. Power measurements and thermal parameter estimates

To demonstrate the zone heating programming and validate the thermal model for the energy estimations, discrete measurements of power were performed for isothermal and linear temperature-ramp separations. A 16-bit DAQ card (USB-6218 OEM, National Instruments, Austin, TX) was used to record the PWM voltage applied to each segment heater at a sampling rate of 250 Hz. The supplied current was measured from the voltage drop across a 1 Ω series resistor. The instantaneous power, P_i, was obtained by taking the product of the voltage and current waveforms. The energy consumption of a given separation experiment was calculated by integrating P_i over the total separation time.

To obtain the thermal parameters of the μcolumn, first C_i and R_i were estimated by placing all three segment heaters in controlled feedback loops and heating them at the same linear ramp rate, M = 10 °C/min, while temperature was simultaneously monitored. When the three temperatures are equal, θ_c/R_c approaches zero and C_i and R_i could be evaluated from the intercept and slope, respectively, of the linear portion of the power-time profile via Eq. (2) when P_{ci} = 0.

To estimate the inter-segment thermal resistance, R_c (Fig. 1), the μcolumn was placed in the GC oven at 30 °C and 1.2 W of power was applied only to the segment 2 heater. After several seconds, all segments came to steady-state temperatures, θ_s. Under these conditions the capacity term in Eq. (2) goes to zero and R_c could be evaluated from P_2, θ_s, θ_c and R_2, using Eq. (4), accounting for the (2×) crosstalk losses to both flanking segments.

3. Results and discussion

3.1. Initial characterization

Fig. 2b–e shows images of the μcolumn: (b) front side and (c) back side photographs of the PCB-mounted device, along with photomicrographs of (d) the center of the first segment and (e) the thermal isolation slots between spiral segments and at the periphery of the chip. Due to the size of the chip, each Si wafer yielded a maximum of only two devices. Owing, apparently, to the grain boundaries of the e-beam evaporated Pt films, their resistances were higher than expected. Therefore, the thickness of the Pt in the heaters and RTDs was increased from 300 to 360 nm to match the modeled target resistance values.

Measured power profiles of segments 1–3 are shown in Fig. S5 (SM). From these, the following values of heat capacity and thermal resistance were determined: $C_1 = C_3 = 0.85$ J/°C, $C_2 = 0.68$ J/°C, $R_1 = R_3 = 42$ °C/W and $R_2 = 72$ °C/W (see caption of Fig. S5). The slightly higher thermal capacities for segments 1 and 3 (*vis a vis* segment 2) can be ascribed to their having three open sides. The lower thermal resistances for segments 1 and 3 can also be explained by the presence of an extra open side, and to the added thermal losses via epoxy connections to the substrate and capillaries. Steady-state heating measurements gave a value of R_c = 30 °C/W. Measured thermal crosstalk among segments was about 56% between adjacent segments, and 32% between the opposite side segments (e.g. for a 30 °C temperature difference above ambient in segment 1, segment 2 increased 16.8 °C and segment 3 increased ~9.6 °C).

From the *n*-octane data used to construct the Golay plot in Fig. S2 of the SM characterizing the efficiency of the PDMS-coated μcolumn, k values ranged from ~4 to 6 and the minimum plate height, H_{min} = 0.026 cm, was obtained at the optimal velocity, $\bar{u}_{opt}$ = 11 cm/s, which corresponds to a volumetric flow rate of 0.24 mL/min of N_2. The maximum plate count, N_{max}, was estimated to be 23,000 plates, or 3800 plates/m. This value is somewhat lower than N_{max} values we have reported previously [27], and, in fact, subsequent μcolumns coated in a similar fashion yielded N_{max} = 4100 plates/m.

For reference, the energy required for a typical analytical cycle with the PEMM prototype was determined experimentally using global μcolumn heating. A 60-s air sample was collected at 5 mL/min, followed by thermal desorption of the micro-preconcentrator/focuser (μPCF) at 225 °C for 40 s. Then, a temperature programmed separation was performed, which entailed holding the μcolumn at 30 °C for 35 s followed by a linear ramp at 40 °C/min to 110 °C and a 5-s hold at that temperature. A re-set period of 3 min was then allowed for cool-down and purging of the inlet. Both the μPCF and the μcolumn returned to the baseline temperature of 30 °C within the 3-min cool-down period. The total cycle was 5.5 min and required 2710 J, including all thermal, pneumatic, and electronic components and functions. Of this total, 475 J (18%) was required for (global) μcolumn heating. If the energy required for electronic components were excluded, then the μcolumn would account for 37% of the total energy (i.e., 475/1283 J), amply justifying efforts to reduce its contribution.

3.2. BTM vs. experimental retention times

The accuracy of the BTM was evaluated by comparing predicted and experimental t_R values for the test compounds under a range of isothermal (i.e., 50–100 °C) and temperature ramped (i.e., 10–60 °C/min) conditions. Complete results are tabulated in Tables S1 and S2 (EM). Representative results at 60 °C (isothermal) and at 40 °C/min (programmed) are presented in Figs. 3a and 3b, respectively. As shown, the errors were quite small, ranging from −0.31 to +2.1 s in Fig. 3a and from −0.57 to +2.4 s in Fig. 3b. In both cases, the errors increased as t_R increased (i.e., as the volatility of the compounds decreased). Among all tests run under isothermal conditions, absolute errors were <1.4 s for the six most volatile compounds and <3.3 s for the three less volatile compounds, with the exception of *n*-decane at the lowest temperature (50 °C) which had an error of −6.1 s. Since the magnitudes of the errors increased with t_R value, the fractional errors were small and the model performed adequately well for all practical purposes.

Among all tests run under temperature ramped conditions, absolute errors were generally higher than for isothermal tests but showed similar trends with compound volatility (i.e., t_R value) and, again, the model performed adequately well for the purposes

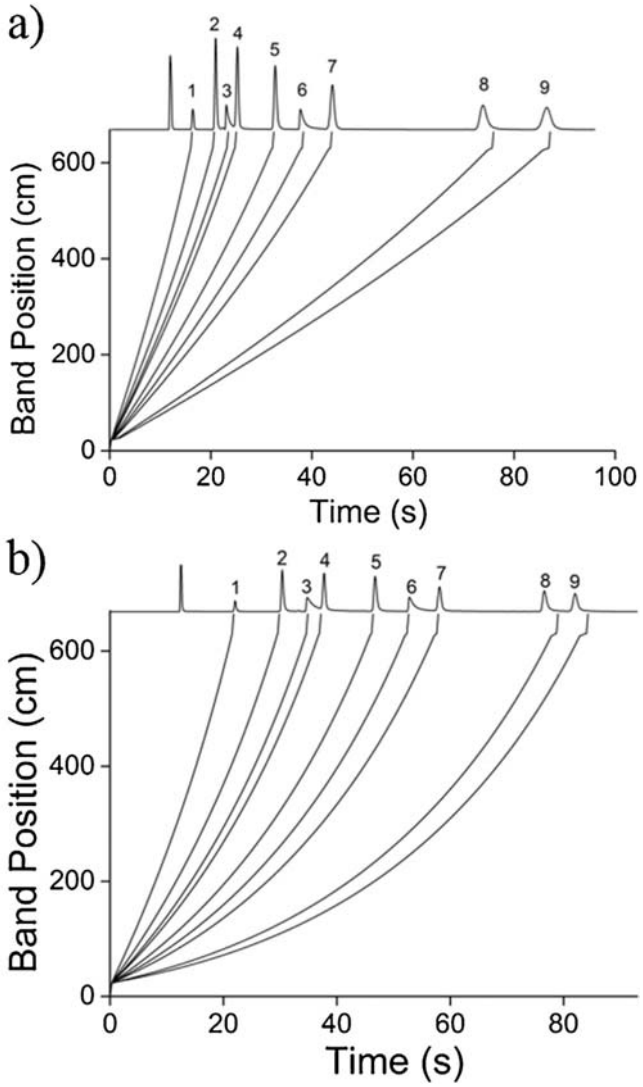

Fig. 3. Experimental chromatograms of the nine test compounds under (a) isothermal (60 °C) and (b) temperature ramped (40 °C/min starting at 30 °C) conditions. Experimental traces are shown across the top of each panel and the BTM-predicted trajectories are shown beneath. GC conditions: ~0.05 μg injection for each compound; 13.5 PSI He inlet pressure; 6-m long PDMS-coated μcolumn; FID. Note: solvent peak (CS_2) appears before peak 1. Identities of peaks 1–9 are given in Table 1.

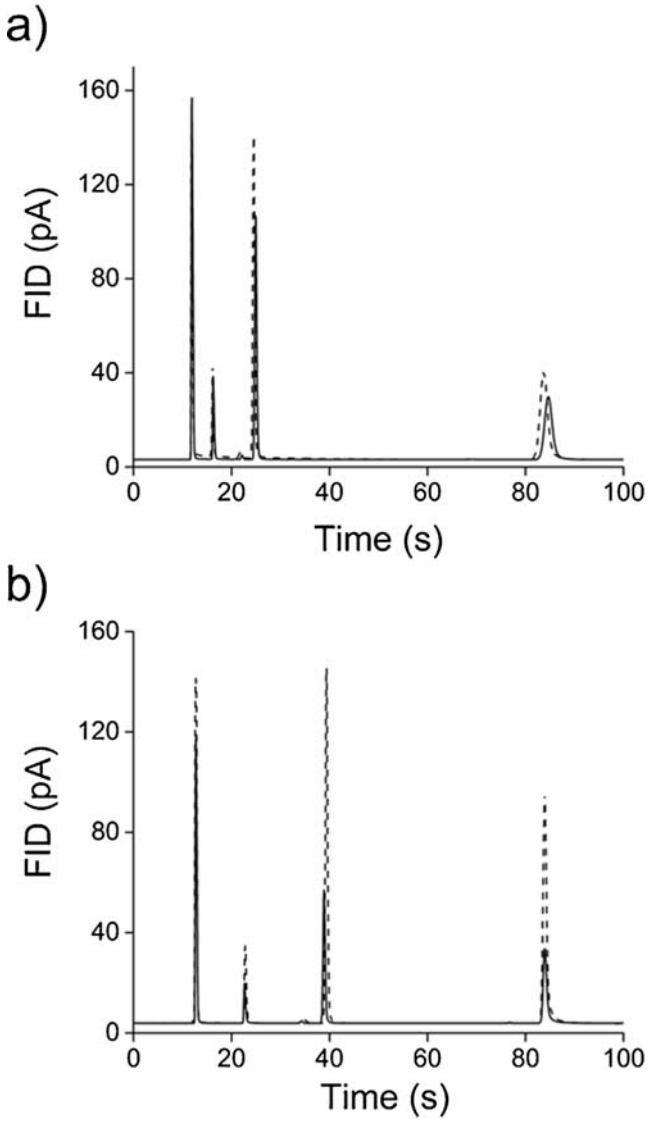

Fig. 4. Superimposed (a) isothermal (60 °C) and (b) temperature ramped (40 °C/min) chromatograms of the "general" subset of compounds (Table 1) with global (solid lines) and zone (dashed lines) heating. The first peak in each trace is solvent (CS_2). In order to see the similarities in t_R values for zone vs. global heating when the traces were superimposed, slightly different injection volumes were used. Zone heating schedule was determined via BTM (see Tables S3 and S4 of the SM for more details).

of guiding segmented heater scheduling. The observed tendency toward negative errors can be ascribed to wall adsorption on interconnecting capillaries, to temperatures being slightly lower than indicated by the RTDs due to small vertical thermal gradients for isothermal cases, and additionally to lags in actual heating rates due to the thermal mass of the μcolumn for temperature ramped cases.

3.3. Separations with global vs. zone heating

Isothermal and temperature programmed separations of each ternary subset mixture designated in Table 1 were performed with zone and global heating. The zone heating schedule was based on BTM. Fig. 4a and b presents representative results for the "general" subset and show that the values of t_R were nearly identical, regardless of the heating method. The complete set of t_R values obtained for all subsets are presented in Tables S3 and S4 (SM) and confirm the close agreement in t_R values in all cases.

3.4. Temporal profiles of temperature and power

Figs. 5a and b show experimental temperature and power profiles, respectively, for global and zone heating of the μcolumn for an isothermal separation at 60 °C, suitable, say, for the low-volatility subset in Table 1 (note: the global temperature profile is not actually shown because it would have obscured the details of the zone heating profiles), but it would correspond to an initial rise along the solid line shown in the plot in Fig. 5a and then a constant temperature for the remainder of the run. Figs. 5c and d show the corresponding profiles for a linear temperature ramped separation from 30 to 83 °C at 40 °C/min (in this case, the global temperature profile corresponded to a linear increase to ~95 s for all segments). The PWM power profiles represent 1-s averages (i.e., they were not smoothed significantly). For the zone-heated isothermal case, the segment 1 heater was turned on a t = 0 and brought up to 60 °C within 9 s (i.e., at 200 °C/min). The turn-on times of the segment 2 and 3 heaters, 20 and 34 s, respectively, were determined

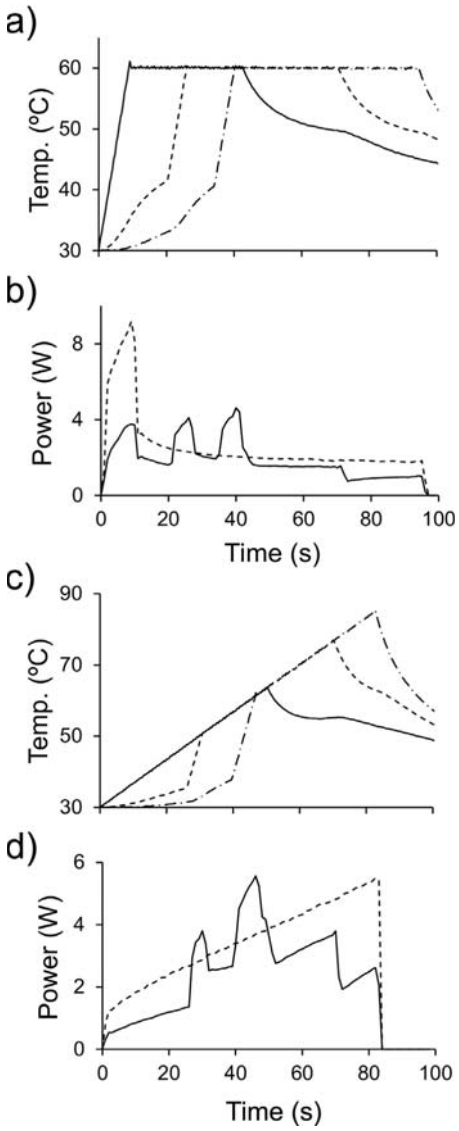

Fig. 5. Measured (a) and (c) temperature profiles and (b) and (d) power profiles of the zone-heated μcolumn for an isothermal separation at 60 °C[(a) and (b)], and a temperature-ramped separation at 40 °C/min [(c) and (d)]. Shown are the temperatures of segment 1 (solid line), 2 (dashed line) and 3 (dot dashed line) of the zone heated μcolumn. Applied instantaneous total power is shown for zone (solid line) and global heating (dashed line). Profiles correspond to conditions suitable for the low volatility subset.

from BTM estimates of the residence times of *n*-nonane (i.e., the earliest eluting component of the mixture) in segments 1 and 2 (see Table S3, SM), after adding the offset required for pre heating the first segment and subtracting the time required to bring the current segment to 60 °C (~6 s for both segment 2 and 3). The corresponding turn-off times for segments 1 and 2 were determined from BTM estimates of the residence times of *n*-decane (the last-eluting component) in segments 1 and 2 and were set at 42 and 70 s, respectively. As shown, control was quite good, as the set point temperature was reached in all cases within ±1 °C and a slight overshoot was only evident for segment 1 (Fig. 5a, solid line). Note that the initial gradual rise in temperature for segments 2 and 3 was due to thermal cross talk from segment 1 over the first ~20 s and from segments 1 and 2 over the first 38 s, respectively.

The power profile for the global heating case (Fig. 5b) showed an initial rapid increase followed by a slower increase to its maximum within 9 s, consistent with PWM control. Having reached the set-point temperature of 60 °C, the power then dropped to a steady-state value of ~2 W, which maintained the μcolumn at 60 °C over the 100-s run. For the corresponding zone heating power profile, there were peaks in power dissipation at the three points in time corresponding to the initial heating of the successive segments followed by a biphasic decline to the levels required to maintain the 60 °C steady-state temperature.

As expected, the peak power required to heat each separate segment was much lower than that required for global heating. After the second power peak, both segments 1 and 2 had to be maintained at 60 °C, so the steady-state power level increased slightly. Since the turn-off time for segment 1 coincided with the turn-on time for segment 3 (Fig. 5a), the third power peak was attenuated. About 1.5 W was required to maintain segments 2 and 3 at steady-state until t = 71 s, when the segment-2 heater was turned off and the power was decreased to the value needed to maintain segment 3 at steady state.

After the segment-3 heater was turned off, the temperature decreased at a rather low rate (Fig. 5a), in part, due to the lack of active cooling within the GC oven. (note: in the PEMM, active cooling is provided by fans that bring all three segment down to baseline temperature within 3 min). It is apparent by visual inspection that the integrated area under the power-time profile for zone heating was less than that for global heating (Fig. 5b). Indeed, for this run, the value of E_R was 0.26.

Fig. 5c shows the corresponding temperature profiles for BTM-guided zone heating of the temperature-ramped separation. The profile for the global heating case would follow the line formed by the combination of zone-heated profiles. Segment 1 was heated from the outset at the designated rate of 40 °C/min. Heat transfer to segments 2 and 3 was, again, evident by the gradual increase in their temperatures prior to their heaters being turned on at 26 and 40 s, respectively. Turn-off times corresponded to the elution of *n*-decane through each segment.

The power profiles (Fig. 5d) followed the expected patterns, where an initial rapid step was required to overcome the thermal capacitance (first term of Eq. (2)) and then a linear increase was required to overcome the heat loss to the environment and adjacent segments while continuously increasing the μcolumn or segment temperature at the specified rate. As with the isothermal cases, the power required early in the run was lower for zone heating, and was primarily driven by C_i and R_i of segment 1 (R_c notwithstanding). The peaks corresponded to the turn-on times of segments 2 and 3, and the latter peak was higher because segment 3 needed to be brought to a higher temperature to keep pace with the ramp. The successive decreases in power at 48 and 70 s corresponded to the turn-off times of segments 1 and 2, respectively. Once again, apparent by visual inspection (Fig. 5d), the energy for zone heating was less than that for global heating (i.e., $E_Z < E_G$). In this case, the value of E_R was 0.27.

3.5. Energy per analysis

Fig. 6 plots the simulated values of energy versus analysis time (t_a) for three different isothermal (Fig. 6a) and temperature ramped (Fig. 6b) separations. Each data point along a given curve is designated by a symbol corresponding to the subset to which it belongs (see Fig. 6 caption). Furthermore, the x-coordinate for each data point corresponds to the time required for elution of the least-volatile component of the given subset mixture, as determined by BTM. For a given temperature condition there are three curves shown, one for global heating (filled symbols, solid curve) and two for zone heating. Of the latter, one (open symbols, dashed curve) entailed all three segment heaters being turned on at the outset, followed by segment 1 and 2 heaters being turned off in sequence as the least volatile compound eluted through them. We refer to

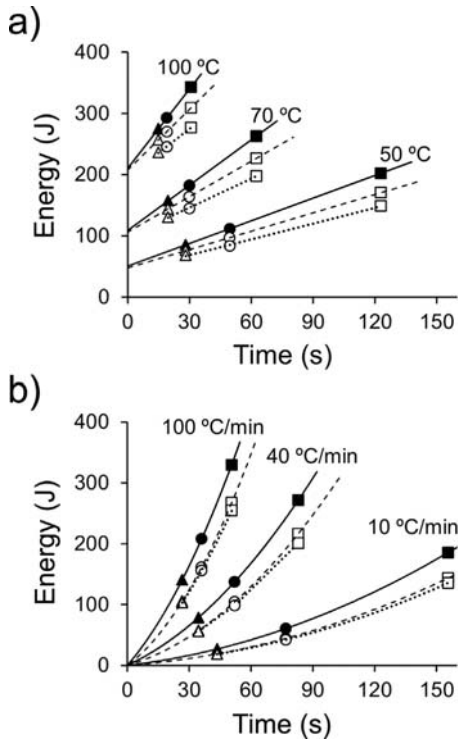

Fig. 6. Simulated energy consumption vs. analysis time for the separation of each subset mixture under different (a) isothermal and (b) temperature ramped separation conditions. The analysis time was defined by the latest eluting compound in each subset: 2-hexanone (high volatility, triangles), 3-heptanone (medium volatility, circles), and *n*-decane (low volatility, squares). Filled symbols and solid lines are for global heating cases; unfilled symbols and dashed lines are for zone heating cases with only early turn-off of segments 1 and 2; and unfilled symbols and dotted lines are for zone heating cases with both early turn-off of segments 1 and 2, and late turn-on of segments 2 and 3.

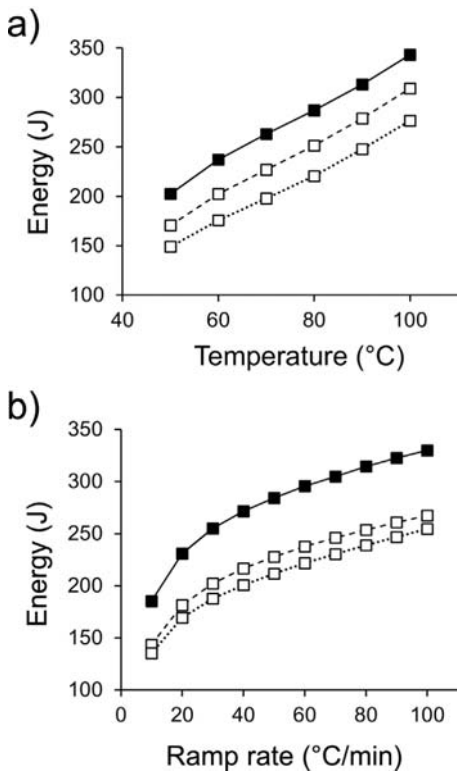

Fig. 7. Simulated energy consumption for the low volatility subset under (a) isothermal conditions and (b) temperature ramped conditions at different temperatures and ramp rates, respectively. Filled squares and solid lines are for global heating; unfilled squares and dashed lines are for zone heating with only early turn-off of segments 1 and 2; open squares with dotted lines are for zone heating with both early turn-off of segments 1 and 2, and late turn-on of segments 2 and 3. The heating times were based on BTM derived retention time values.

this below as the "early-off" scenario. The other zone heating scenario (open symbols, dotted curve) entailed each segment heater being turned on and then turned off on a schedule dictated by the residence times of the eluting compounds within that segment. We refer to this as the "late-on/early-off" scenario.

As expected from Eqs. (3) and (5), and as observed in Figs. 6a and b, the time dependence of the energy consumption is linear for the isothermal separations and quadratic for the temperature ramped separations. The y-intercept of each curve in Fig. 6a corresponds to the $C_i\theta_s$ term from Eq. (3), which increases with increasing set-point temperature and contributes equally to the energy for all heating scenarios at a given set point. As a result, its fractional contribution to the total energy varies directly with the volatility of the subset. For example, at 50 °C, it is ~60% of the total energy for the high volatility subset (triangles) but only ~25% of the total energy for the low-volatility subset (squares). Hence, the energy *saved* by use of zone heating will vary inversely with the volatility of the subset (i.e., high < medium < low) for isothermal separations. This is not the case for temperature ramped separations (Fig. 6b) because the capacitance term contributes continuously to the energy consumed throughout the separation.

The higher the set-point temperature (Fig. 6a) or ramp rate (Fig. 6b), the greater the energy consumed for the separation, in spite of the shorter total elution times (i.e., smaller value of t_a). But the *dependence* on set-point temperature or ramp rate varies with subset volatility in the order low < medium < high, which is apparent by looking at the same symbol across different temperatures or ramp rates, regardless of whether global or zone heating is used. For example, in Fig. 6b, the ratio of energies consumed at 100 °C/min and 10 °C/min for the zone-heated separation of the high-volatility subset (open triangles) is ~103 J/19 J or about ~5 fold, whereas for the low-volatility subset (open squares) it is 255 J/135 J, or only ~2 fold. In all cases, however, the energy consumed with zone heating is less than that with global heating.

The extent of energy savings from zone heating bears closer examination. As shown in Figs. 6a and b, and highlighted further with the example in Fig. 7a and b, the specific zone-heating scenario employed affects the energy saved to a greater degree for isothermal separations than for temperature ramped separations. For all isothermal set-point temperatures, the energy reduction for the "early-off" zone-heating scenario is about 55% of that for the "late-on/early-off" scenario. This is true for all analyte subsets, and is shown clearly in Fig. 7a, for the specific example of the low-volatility subset. In contrast, for the temperature-ramped separations, regardless of the ramp rate, the energy reduction for the "early off" zone-heating scenario is about 82% of that for the "late-on/early-off" scenario. That is, the reduction in energy for zone (vs. global) heating is predominated by turning off the heaters for segments 1 and 2 as soon as they are no longer contributing to the separation. This, in turn, indicates that the residence times of the latest eluting component of a mixture (i.e. typically that with the lowest p_v value) in the first two segments of the μcolumn dictate the energy reduction achievable with zone heating in a temperature ramped separation.

To probe this matter further, Fig. 8 presents the ratio of the residence (or retention) time in segment 1, t_{R1}, to the total analysis time (t_a) under isothermal and temperature-ramped conditions for the least volatile component of each subset mixture. For isothermal conditions (Fig. 8a), the ratio was about 0.4 and there was very little difference among the subsets or across the set-point temper-

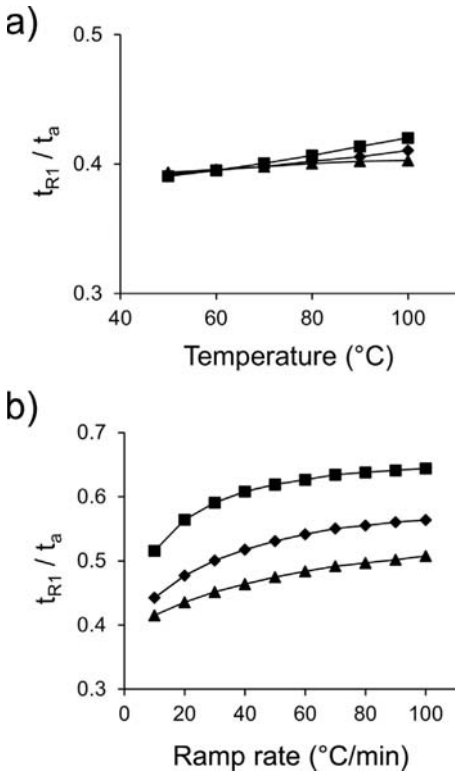

Fig. 8. Simulated fraction of time spent by a compound in the first μcolumn segment as a function of (a) isothermal temperature and (b) ramp rate. This variable is a measure of the curvature of the band trajectory. Triangles: 2-hexanone; diamonds: 3-heptanone; and squares: *n*-decane.

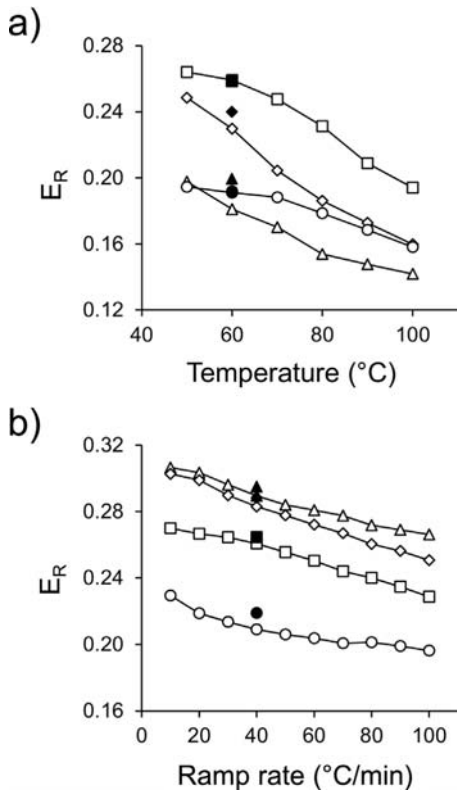

Fig. 9. Fractional energy reduction, E_R, due to zone (vs. global) heating of the μcolumn for (a) isothermal and (b) temperature ramped separations of different compound subsets: high volatility (triangles), medium volatility (diamonds), low volatility (squares), and general (circles). Unfilled symbols represent simulated data and filled symbols represent experimental data.

atures. This is a reflection of the linearity of the band trajectories (see Fig. 3a). In contrast, for the temperature-ramped conditions the t_{R1}/t_a ratio increased monotonically with ramp rate and also increased with the p_v values of the three analytes. These trends arise from the curvature of the band trajectories under temperature-ramped conditions (Fig. 3b), and from the different degrees of curvature that arise as a function of both the ramp rate and analyte volatility.

Since the relative amount of time spent in segment 1 (and, thus, segment 2) differed markedly, so, too, did the impact of the specific zone-heating scenario. In all cases, the time spent in a given segment was in the order segment 1 > segment 2 > segment 3. Furthermore, since the lower volatility compounds spent relatively (and absolutely) more time in segment 1 than the high volatility compounds, the energy reduction was smaller for the low volatility subset. That is, since the segment 1 heater could be turned off earlier in the separation of the higher volatility subsets, it spent relatively more time off than it did in the separation of the low volatility subset. Also, across all subsets, the energy reduction decreased with increasing ramp rate, for the same reason.

Figs. 9a and b compare values of energy reduction, E_R, for isothermal and temperature-ramped separations, respectively, of all four subset mixtures. Experimental E_R values (filled symbols) differed from modeled E_R values (unfilled symbols) by −0.1 to 1.8% for isothermal conditions and by −0.1 to 1.2% for temperature ramped conditions, i.e., they were generally slightly higher than the modeled values. For isothermal separations, the energy saved by use of zone heating (i.e., with the "late-on/early-off" scenario) decreased as the temperature increased and as the volatility of the mixture components increased, consistent with the data in Fig. 6a. That is, the mixture requiring the longest time for separation yielded the most savings, with the largest E_R value in this data set estimated to be ~26%, at the lowest temperature of 50 °C for the lowest volatility subset.

Fig. 9a also shows that the energy reductions for the general subset fell between those of the high and medium subsets and had less of a temperature dependence. This is because of the wider range of volatility spanned by this subset and the corresponding demands for longer segment heating times. For the temperature ramped cases in Fig. 9b, the reductions in energy with zone heating were greater than those for isothermal cases. In these cases, however, high and medium volatility subsets yielded greater energy reductions than did the low volatility and general subsets, which is expected from the BTM curvature differences seen in Fig. 8b.

The range of E_R values among all conditions and subsets in Fig. 9 is 14–31%. For a given subset a larger range of values was spanned for isothermal separations across the different temperatures than for temperature ramped separations across the ramp rates examined. In all cases, the price paid for more rapid elution times was smaller energy savings, with the amount depending on the mixture components and time of analysis. Regardless of the specific value of E_R, the energy savings was significant.

4. Conclusions

From the results reported here, we conclude that zone heating of this novel segmented μcolumn can afford significant energy savings without sacrificing chromatographic resolution or analysis time relative to global heating of the entire chip. The energy saved is a function of the structure of the device and materials of construction, the heating profile employed in the separation, and the absolute and relative vapor pressures of the analytes in the mixture being separated. For the limited data set generated

here the fractional reduction in energy due to zone heating ranged from 14 to 31%. Since μcolumn heating can account for >35% of the energy consumed by the fluidic components of a wearable μGC, such as the PEMM prototype we have developed, a net reduction of ~5-10% in the energy per analysis could be realized (electronics notwithstanding), with a corresponding increase in battery life.

The measures taken here to thermally isolate the segments still allowed thermal cross talk of 56% between adjacent segments. Furthermore, the substrate and cover plate used were rather thick (i.e., 500 and 200 μm, respectively). Additional efforts to reduce the mass of the device and to improve thermal isolation (i.e., to increase R_c) would lead to improvements in energy savings. The substrate thickness is currently constrained by the need for edge-wise connections to capillaries having outer dimensions >300 μm. The use of Si as the substrate offers advantages of well-established machining methods such as DRIE. Its thermal conductivity reduces thermal gradients and thermal response times, but also increases cross talk. On balance, Si would seem to be a suitable substrate. Although we have found Pyrex wafers to become fragile below a thickness of 200 μm, post-bond polishing might be used to reduce the thickness by a substantial fraction with less risk of fracture.

Integral to this concept is the use of BTM and the associated need for temperature dependent k values of all analytes, which increases the overhead associated with implementing this technique. However, since the temperature dependence of retention factors, particularly with PDMS stationary phases, is predictable, it should be possible to collect a minimum of reference data points (e.g., at, say, two temperatures) and to then interpolate or extrapolate k values with sufficient accuracy to implement BTM and, thus, to schedule the zone heating required for separation of even moderately complex vapor mixtures.

In follow-on work, we plan to explore the extent to which zone heating might enhance peak capacity while simultaneously minimizing analysis time. The capability for rapidly and precisely ramping the segment temperatures should facilitate such efforts. Since we have installed these μcolumns in the PEMM prototypes we are currently testing, any enhancements we might discover could be readily put into practice in a field-ready, wearable unit.

Acknowledgments

The authors wish to thank Mr. Changhua Zhan and Prof. Xudong Fan for assistance in collecting photographic images of the μcolumn chip. Funding was provided by the National Institute for Occupational Safety and Health of the Centers for Disease Control and Prevention (Grant R01-OH-010297). The authors are solely responsible for the content of this article. Devices were made in the Lurie Nanofabrication Facility.

Appendix A. Supplementary data

Supplementary data associated with this article can be found, in the online version, at http://dx.doi.org/10.1016/j.snb.2017.07.065.

References

[1] R.L. Grob, E.F. Barry, Modern Practice of Gas Chromatography, 4th ed., Wiley Interscience, Hoboken, NJ, 2004.
[2] PerkinElmer Torion Technologies Inc. http://torion.com/home.html (Accessed August 2016).
[3] Inficon, Inficon 3000 Product Information. http://products.inficon.com/en-us/Product/Detail/3000-Micro-GC-Gas-Analyzer?path=Products%2Fpg-ChemicalDetection (Accessed April 2017).
[4] Defiant Technologies, www.defiant-tech.com (Accessed April 2017).
[5] Electronic Sensor Technology, www.estcal.com (Accessed April 2017).
[6] APIX Technologies http://apixtechnology.com (Accessed April 2017).
[7] SEER Technologies http://www.seertechnology.com (Accessed April 2017).
[8] Inficon, Hapsite ER Product Information. http://products.inficon.com/en-us/nav-products/Product/Detail/HAPSITE_ER_Identification_System?path=Products%2Fpg_ChemicalDetection%2F (Accessed August 2016).
[9] C.-J. Lu, W.H. Steinecker, W.-C. Tian, M. Agah, J.A. Potkay, H.K.L. Chan, R.D. Sacks, K.D. Wise, S. Pang, E.T. Zellers, First-generation hybrid MEMS gas chromatograph, Lab Chip 5 (2005) 1123.
[10] P.R. Lewis, R.P. Manginell, D.R. Adkins, R.J. Kottenstette, D.R. Wheeler, S.S. Sokolowski, D.E. Trudell, J.E. Byrnes, M. Okandan, J.M. Bauer, R.G. Manley, G.C. Frye-Mason, Recent advancements in the gas-phase μChem Lab, IEEE Sens. J. 6 (2006) 784.
[11] S. Zampolli, I. Elmi, F. Mancarella, P. Betti, E. Dalcanale, G.C. Cardinali, M. Severi, Real-time monitoring of sub-ppb concentrations of aromatic volatiles with MEMS-enabled miniaturized gas-chromatograph, Sens. Actuator B 141 (2009) 322.
[12] A. Garg, M. Akbar, E. Vejerano, S. Narayanan, L. Nazhandali, L.C. Marr, M. Agah, G.C. Zebra, A mini gas chromatography system for trace-level determination of hazardous air pollutants, Sens. Actuator B 212 (2015) 145.
[13] M. Akbar, M. Restaino, M. Agah, Chip-scale gas chromatography: from injection through detection, Microsyst. Nanoeng. 1 (2015) 15039.
[14] Y.T. Qin, Y.B. Gianchandani, iGC1: an integrated fluidic system for gas chromatography including knudsen pump, preconcentrator, column, and detector microfabricated by a three-mask process, J. Microelectromech. Syst. 23 (2014) 980.
[15] W.R. Collin, K.W. Scholten, X. Fan, D. Paul, K. Kurabayashi, E.T. Zellers, Polymer-coated micro-optofluidic ring resonator detector for a comprehensive two-dimensional gas chromatographic microsystem: μGC×μGC−μOFRR, Analyst 141 (2016) 261.
[16] S.K. Kim, D.R. Burris, H. Chang, J. Bryant-Genevier, E.T. Zellers, Microfabricated gas chromatograph for on-site determinations of trichloroethylene in indoor air arising from vapor intrusion, part 1: field evaluation, Environ. Sci. Technol. 46 (2012) 6065.
[17] W.R. Collin, G. Serrano, L.K. Wright, H. Chang, N. Nuñovero, E.T. Zellers, Microfabricated gas chromatograph for rapid, trace-level determinations of gas phase explosive marker compounds, Anal. Chem. 86 (2014) 655.
[18] S. Terry, H. Jerman, J. Angell, A gas chromatographic air analyzer fabricated on a silicon wafer, IEEE Trans. Electron Devices 26 (1979) 1880.
[19] R.P. Manginell, J.M. Bauer, M.W. Moorman, L.J. Sanchez, J.M. Anderson, J.J. Whiting, D.A. Porter, D. Copic, K.E. Achyuthan, A monolithically-integrated μGC chemical sensor system, Sensors 11 (2011) 6517–6532.
[20] G. Lambertus, A. Elstro, K. Sensenig, J. Potkay, M. Agah, S. Scheuering, K. Wise, F. Dorman, R. Sacks, Design, fabrication and evaluation of microfabricated columns for gas chromatography, Anal. Chem. 76 (2004) 2629.
[21] J. Liu, N.K. Gupta, K.D. Wise, Y.B. Gianchandani, X. Fan, Demonstration of motionless Knudsen pump based micro-gas chromatography featuring micro-fabricated columns and on-column detectors, Lab Chip 11 (2011) 3487.
[22] C.M. Matzke, R.J. Kottenstette, S.A. Casalnuovo, G.C. Frye-Mason, M.L. Hudson, D.Y. Sasaki, R.P. Manginell, C.C. Wong, Microfabricated silicon gas chromatographic microchannels: fabrication and performance, in: Proceedings of Micromachining and Microfabrication Process Technology IV, Santa Clara, CA, USA, 1998, pp. 262–268.
[23] J.A. Potkay, G.R. Lambertus, R.D. Sacks, K.D. Wise, A low-power pressure-and temperature-programmable micro gas chromatography column, J. Microelectromech. Syst. 16 (2007) 1071.
[24] M. Agah, J.A. Potkay, G. Lambertus, R. Sacks, K.D. Wise, High-performance temperature-programmed microfabricated gas chromatography columns, J. Microelectromech. Syst. 14 (2005) 1039–1050.
[25] A. Bhushan, D. Yemane, D. Trudell, E.B. Overton, J. Goettert, Fabrication of micro-gas chromatograph columns for fast chromatography, Microsyst. Technol. 13 (2007) 361.
[26] H. Noh, P.J. Hesketh, G.C. Frye-Mason, Parylene gas chromatographic column for rapid thermal cycling, J. Microelectromech. Syst. 11 (2002) 718.
[27] A.D. Radadia, R.D. Morgan, R.I. Masel, M.A. Shannon, Partially buried microcolumns for micro gas analyzers, Anal. Chem. 81 (2009) 3471.
[28] G. Serrano, S.M. Reidy, E.T. Zellers, Assessing the reliability of wall-coated microfabricated gas chromatographic separation columns, Sens. Actuators B 141 (2009) 217.
[29] D. Gaddes, J. Westland, F.L. Dorman, S. Tadigadapa, Improved micromachined column design and fluidic interconnects for programmed high-temperature gas chromatography separations, J. Chromatogr. A 1349 (2014) 96.
[30] S. Ali, M. Ashraf-Khorassani, L.T. Taylor, M. Agah, MEMS-based semi-packed gas chromatography columns, Sens. Actuator B 141 (2009) 309.
[31] J. Wang, Z. Lin, N. Nuñovero, R. Nidetz, S. Buggaveeti, K. Kurabayashi, W.H. Steinecker, E.T. Zellers, A wearable MEMS gas chromatograph for multi-vapor determinations, Proc. Eng. 168 (2016) 1398–1401.
[32] S.K. Kim, H. Chang, E.T. Zellers, Microfabricated gas chromatograph for the selective determination of trichloroethylene vapor at sub-parts-per-billion concentrations in complex mixtures, Anal. Chem. 83 (2011) 7198.
[33] W.R. Collin, A. Bondy, D. Paul, K. Kurabayashi, E.T. Zellers, μGC × μGC: comprehensive two-dimensional gas chromatographic separations with microfabricated components, Anal. Chem. 87 (2015) 1630.
[34] M. Zhou, J. Lee, H. Zhou, R. Nidetz, K. Kurabayashi, X. Fan, A fully automated portable gas chromatography for sensitive and rapid quantification of volatile organic compounds in water, RSC Adv. 6 (2016) 49416.
[35] J. Lee, M. Zhou, H. Zhou, R. Nidetz, K. Kurabayashi, X. Fan, In situ calibration of micro-photoionization detector in multi-dimensional micro-gas chromatography system, Analyst 141 (2016) 4100.

[36] B. Chen, T. Hung, R. Jian, C.-J. Lu, A multidimensional micro gas chromatograph employing a parallel separation multi-column chip and stop-flow μGC × μGCs configuration, Lab Chip 13 (2013) 1333.
[37] A.Z. Wang, S. Hynynen, A.R. Hawkins, S.E. Tolley, H.D. Tolley, M.L. Lee, Axial thermal gradients in microchip gas chromatography, J. Chromatogr. A 1374 (2014) 216–223.
[38] M. Navaei, A. Mahdavifar, J. Dimandja, G. McMurray, P. Hesketh, All silicon micro-GC column temperature programming using axial heating, Micromachines 6 (2015) 865–878.
[39] M. McGuigan, R.D. Sacks, Band-trajectory model for temperature-programmed series-coupled column ensembles with pressure-tunable selectivity, Anal. Chem. 73 (2001) 3112.
[40] R.C. Weast, CRC Handbook of Chemistry and Physics, 49th ed., The Chemical Rubber Co, Cleveland, 1968.
[41] S.A.W. van Herwaarden, in: G.C.M. Meijer (Ed.), Smart Sensor Systems, Wiley, Chichester, UK, 2008, Thermal Sensors, 151.
[42] G. Sidebotham, Heat Transfer Modeling: An Inductive Approach, Springer, New York, NY, 2015.
[43] Pubchem https://pubchem.ncbi.nlm.nih.gov/ (Accessed April 2017).

Biographies

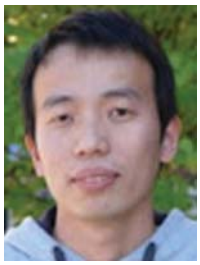

Zhijin Lin earned B.S. and M.S. degrees in Chemistry from Fuzhou University in China. He earned a Ph.D. degree in Analytical Chemistry from Wayne State University in 2015. He then worked with Professor Zellers as a research fellow at the University of Michigan, focusing on the research and development of μGC instrumentation for VOC analysis. He is currently employed as a senior analytical scientist at AAK China, Ltd.

Nicolás Nuñovero earned a B.S. degree in Electronic Engineering from the Pontifical Catholic University of Peru in 2006. He is currently working with Professor Zellers at the University of Michigan on the development and characterization of μGC devices and systems. His current research interests include low-noise, low-power, mixed-signal interfaces and control software for MEMS-based systems.

Junqi Wang earned a B.S. in Chemistry from the University of Nebraska, Kearney in 2013, and is currently pursuing a Ph.D. in Chemistry at the University of Michigan, under the advisement of Professor Zellers. His research focuses on the development and characterization of novel materials and MEMS-based micro-devices and micro-analytical instrumentation for airborne and aqueous volatile organic compound (VOC) determinations.

Robert Nidetz received a B.S. in Materials Science and Engineering with minors in Chemistry and Business Administration from the University of Illinois at Urbana/Champaign in 2006. He received his M.S. (2009) and Ph.D. (2011) in Materials Science and Engineering from the University of Michigan, Ann Arbor where he investigated the self-assembly of nanogold for optical meta-materials. After spending time working in the MEMS industry, he returned to the University of Michigan as a postdoc in Prof. Kurabayshi's laboratory where he designed and fabricated components for μGC systems and microfluidic devices for medical diagnostics. He is currently a Research Associate in Prof. Kurabayashi's group where he is a consultant to develop silicon-based MEMS devices.

Sanketh Buggaveeti received a B.S. in Mechanical Engineering with a specialization in energy systems from Vellore Institute of Technology, India, in 2012. He received an M.S. in Mechanical Engineering at the University of Michigan in 2014, working with Prof. Kurabayashi on the design and finite element simulation of integrated μGC systems. He is currently working on the next generation of multi terabit optical communication systems as a Hardware Development Engineer at Infinera.

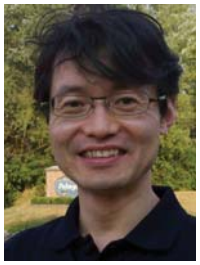

Katsuo Kurabayashi is Professor of Mechanical Engineering and Electrical Engineering and Computer Science at the University of Michigan, Ann Arbor. He received his BS in Precision Engineering from the University of Tokyo in 1992, and his MS and PhD in Materials Science and Engineering from Stanford University, CA, in 1994 and 1998, respectively. His current research focuses on optofluidics, nanoplasmonic and biomolecular biosensing, and microsystems for immunology, clinical diagnosis, and analytical chemistry. He received the 2001 NSF Early Faculty Career Development (CAREER) Award, the Robert Caddell Memorial Award in 2005, the Pi Tau Sigma Outstanding Professor Award in 2007, the Mechanical Engineering Outstanding Achievement Award in 2013 from the University of Michigan, and the Ted Kennedy Family Team Excellence Award in 2015 from the College of Engineering at the University of Michigan.

Edward T. Zellers (B.A. Chemistry, Rutgers; MS, PhD, Environmental Health Sciences, University of California, Berkeley) joined the faculty at the University of Michigan in 1987 and is currently appointed as a Professor in the Department of Environmental Health Sciences (EHS) and in the Department of Chemistry. He is Director of the Occupational Health Program in EHS. From 2000 to 2016, he was the Leader of the Environmental Sensors and Systems Thrust in the Michigan Center for Wireless Integrated MicroSensing and Systems (WIMS^2). He has been involved in research on chemical microsensors and micro-instrumentation for volatile organic compounds for over 30 years, with particular interests in the design and physicochemical characterization of devices and materials related to the capture, preconcentration, separation, and sensing of multi-vapor mixtures. In 2010, he received both the Outstanding Teacher Award from the School of Public Health and the Ted Kennedy Family Team Excellence Award from the College of Engineering.